Modeling of Complex Parison Formation in Extrusion Blow Molding: Effect of Medium to Large Die Heads and Fuel Tank Geometry

Yousefi, Azizeh-Mitra; Atsbha, Haile

Publisher's version / la version de l'éditeur:
Polymer Engineering and Science, 49, 2, pp. 229-239, 2009-02-01

Web page / page Web
http://dx.doi.org/10.1002/pen.21243
http://nparc.cisti-icist.nrc-cnrc.gc.ca/npsi/ctrl?action=rtdoc&an=11343978&lang=en
http://nparc.cisti-icist.nrc-cnrc.gc.ca/npsi/ctrl?action=rtdoc&an=11343978&lang=fr

Modeling of Complex Parison Formation in Extrusion Blow Molding: Effect of Medium to Large Die Heads and Fuel Tank Geometry

Azizeh-Mitra Yousefi[1*] and Haile Atsbha[2]

1) Industrial Materials Institute (IMI), National Research Council of Canada, Boucherville, Quebec, J4B 6Y4, Canada

2) *Kautex Inc., Windsor, Ontario, N8W 5B1, Canada*

[*]Corresponding author; email: azizeh.yousefi@imi.cnrc-nrc.gc.ca

Modeling of Complex Parison Formation in Extrusion Blow Molding: Effect of Medium to Large Die Heads and Fuel Tank Geometry

Azizeh-Mitra Yousefi[1] and Haile Atsbha[2]

1) Industrial Materials Institute (IMI), National Research Council of Canada, Boucherville, Quebec, J4B 6Y4, Canada

2) Kautex Textron Inc., Windsor, Ontario, N8W 5B1, Canada

ABSTRACT

In extrusion blow molding, the complexity of the part geometry could dictate the use of advanced manufacturing technologies to meet the target part thickness requirements. In standard extrusion blow molding, the parison axial thickness distribution is controlled using a vertical wall distribution system (VWDS). This is achieved by manipulating the die gap opening at a given number of programming points. However, this technique may not be sufficient to produce the desired outcome in the manufacturing of highly complex fuel tank shapes driven by design constraints of available irregular design space and the ever increasing demand of increasing fuel capacity. Hence, the manufacturing of these complex part shapes may require the use of advanced die shaping technologies such as die slide motion (DSM) and partial wall distribution system (PWDS). The PWDS technology allows efficient circumferential parison wall thickness control according to a predetermined profile for an optimal part thickness distribution and the lightest part weight. As the parison thickness has a highly non-linear relationship with die gap opening due to the extrudate swell phenomenon, a considerable amount of time, cost and skill is required to get the desired parison dimensions upon any variations in the die geometry and operating conditions. Furthermore, the PWDS technology comes at a substantial increase in capital cost, which adds to the cost of manufacturing. Hence, the accurate assessment of tooling requirement using predictive techniques is imperative to minimize tooling change cost and customer delivery time. In this work, the *BlowParison* software from IMI is used to predict the parison formation accounting for swell, sag, and non-isothermal effects. Since the accurate prediction of parison formation is the key step to the proper modeling of the remaining process phases, emphasis is placed on experimental validation of the predicted parison dimensions using four diverging die geometries and different sets of VWDS/PWDS profiles. A good agreement was found between predicted parison length and weight profiles and experimental data.

Keywords: extrusion blow molding, parison swell, fuel tank, die geometry, die head size, finite element modeling

INTRODUCTION

Extrusion blow molding is a low-cost and efficient manufacturing technique for complex hollow parts (1), including automotive fuel tanks. This process consists of three main phases, namely, parison formation, parison inflation, and part cooling and solidification (2). The parison formation is the most critical phase as the parison dimensions strongly affect the final part thickness distribution and its mechanical performance. Parison swell and sag are factors that significantly influence the parison dimensions, and are strongly affected by die geometry, resin characteristics, and operating conditions. This could lead to a considerable amount of time and cost through trial and error runs to get the desired parison dimensions upon any variations in the processing parameters, in particular for complex parison formation using the VWDS in conjunction with PWDS technique. The availability of a modeling technique ensures a more accurate prediction of the entire blow molding process, as the proper prediction of the parison formation is an input for the remaining process phases.

Parison swell is a result of molecular orientation generated during the flow in the die (3). A combination of elongational and shear stresses are applied to the molten polymer as it travels through the die. Once the melt exits the die in the form of a parison, the stress is relieved and the swell occurs. The parison sag is a result of parison stretching under gravitational forces. The degree of swell and sag is controlled by die design, resin characteristics (e.g. extensional viscosity and damping coefficients), and processing parameters, such as melt temperature, suspension time, and total parison length (4).

Parison swell is defined as an increase in the cross sectional area of the extruded parison, and is represented in terms of the diameter swell (B_1) and the thickness swell (B_2) defined as:

$$B_1 = \frac{D_{parison}}{D_{die}} \tag{1}$$

$$B_2 = \frac{h_{parison}}{h_{die}} \tag{2}$$

where $D_{parison}$ and D_{die} are the parison and die diameters, $h_{parison}$ is the parison thickness, and h_{die} is the die gap opening. The final part thickness distribution is directly related to both diameter swell and thickness swell (5). Therefore, these two parameters can be combined to define the area swell as follows:

$$B_{area} = B_1 \times B_2 \tag{3}$$

A pinch-off mold, originally proposed by Sheptak and Beyer (6) can be used to estimate the diameter and thickness swell in Eqs. 1-2. For simple blow-molded parts, it is shown in a previous study that the weight swell from the dissected final part can efficiently represent the combined effect of the diameter and thickness swell, in the same manner as the area swell (7). Therefore, the weight swell can be estimated as follows when the pinch-off mold measurement is not available:

$$B_w = \frac{w}{w_0} \tag{4}$$

In this equation, w is the weight of the dissected section after swell and sag while w_0 is the corresponding weight of a section without swell and sag, featuring the same length and assuming a cylindrical geometry.

The main contribution to the extrudate swell comes from the memory effect. This is primarily the elastic response to the elongational stresses prevailing at the entrance of the die and, to some extent, to the shear stresses imposed on the melt in the flow channel. Koopmans (8-10) has reported that the maximum swell and the time to reach this value are very sensitive to the molecular weight distribution of the resin. Moreover, according to his findings, small variations in the die geometry are usually much more effective in altering the swelling characteristics of an HDPE resin than most of the operating parameters. Given the non-linear relationship between parison swell and die gap opening observed in previous studies (7,11-13), the experimental data collected at a wide range of die geometries, resin characteristics, and operating conditions can be the most efficient technique to validate the finite element simulations, and to verify the practical validity of the viscoelastic constitutive equations and the mathematical swell models (10).

The main goal of this work is to investigate the effect of die geometry and die gap manipulation on swell and sag for complex parisons produced by a combination of VWDS and PWDS techniques. The collected experimental data are compared with the numerical prediction of the parison formation, performed using *BlowParison* software developed at IMI. Since it is well established that small differences in die geometry can lead to significant swell differences (7,10), it is very important to study the performance of *BlowParison* software in predicting the parison dimensions upon any variation in die geometry and die gap profile. This software has been successfully used in the past to model the swell and sag, combined with the non-isothermal effects, for several industrial parts including fuel tanks (14,15). The software couples a fluid mechanics approach to represent the die flow, with a solid mechanics approach to represent the parison behavior outside the die, and a mathematical swell model to account for the pronounced elongational and shear stresses at high Weissenberg numbers. The fundamentals of this modeling tool can be found elsewhere (7,16).

THEORETICAL BACKGROUND

Manipulation of Die Gap Profile

The final part thickness distribution is directly related to both the diameter swell and thickness swell. For equivalent parison thicknesses, a section with a smaller diameter will result in a section with a thinner final part thickness (17). To satisfy the design constrains for complex parts, e.g. fuel tanks, parison thickness distribution should be controlled using different techniques, so that the final wall thickness of the blown part is as uniform as possible after inflation (17). While the die gap programming (VWDS) allows a desired distribution along the extrusion axis, the irregular shape of the final part requires circumferential parison wall thickness control. To this end, the SFDR, PWDS, and DSM techniques are used in the industry. The die gap manipulation techniques are briefly discussed in the following section.

Vertical Wall Distribution System (VWDS). The desired vertical variation in parison thickness can be attained by VWDS, as schematically illustrated in Fig. 1a. The conical core part (mandrel) is axially shifted relative to the die ring (bushing) during parison formation, leading to the desired die gap opening at a given moment during extrusion. The parameters used in the industry to control the die gap opening are shown in Fig. 1b. The die gap for a given programming point (h_{die}) is calculated based on the stroke parameters defined in Fig. 1b as follows:

$$h_{die} = h_{\min} + \tan(\phi_m) \cdot S_{total} \tag{5}$$

$$S_{total} = S_{\max} \cdot \left[\left(\frac{P_{basic}}{100} \right) + \left(\frac{P_{prog}}{100} \right) \cdot \left(\frac{P_{select}}{100} \right) \right] \tag{6}$$

where:

$$P_{basic} = (100) \cdot \left(\frac{S_{basic}}{S_{\max}} \right) \tag{7}$$

$$P_{prog} = (100) \cdot \left(\frac{S_{prog}}{S_{\max}} \right) \tag{8}$$

$$P_{select} = (100) \cdot \left(\frac{S_{\max} - S_{\lim it}}{S_{\max}} \right) \quad ; \quad P_{select} \le 100 - P_{basic} \tag{9}$$

In these equations, h_{min} is the minimum gap at the machine setting where the mandrel and bushing are in flush configuration, and ϕ_m is the mandrel angle from vertical. As it can be seen from Fig. 1b, the VWDS stroke parameters S_{total}, S_{basic}, S_{prog}, and S_{limit} are in mm while P_{basic}, P_{prog}, and P_{select} are in percentage. The definition of these parameters is consistent with machine parameters used in the industry. Figures 1c and 1d schematically show the position of the mandrel for 0% and 100% die gap programming, respectively. It should be mentioned that a P_{basic} = 0% corresponds to a machine setting where the mandrel and bushing are in flush configuration at 0% die gap programming ($h_{die} = h_{min}$).

Static Flexible Deformable Ring (SFDR). This technique is used in the industry to offer a circumferential variation in parison wall thickness without permanent shaping or profiling of the tooling. In particular, for producing nonsymmetrical parts or square bottles, the thin corners in the final part can be avoided by SFDR. However, it only creates a fixed pre-set circumferential wall thickness distribution throughout the whole parison length (16), as schematically shown in Fig. 2. For complex parts, the uniform thickness requirements can be better satisfied once this technique is combined with the PWDS technology.

Partial Wall Distribution System (PWDS). The need for creating a circumferential variation in the thickness at a specific section along the parison length is the driver of this technology. The pulling

and/or pushing actions (strokes) can be achieved at every desired point, circumferentially and axially (17), as illustrated in Figs. 3a to 3c. Fig. 3d shows the typical variation in the die gap, corresponding to the PWDS action in Fig. 3c. The thin areas in the corners and in the deep-draw sections of the final part can be avoided by using this technique.

Die Slide Motion (DSM). Similar to the PWDS technique, the DSM creates a circumferential variation in the thickness at a specific section along the parison length. However, the pulling and/or pushing actions do not affect the zones outside the DSM stroke action, as illustrated in Figs. 4a and 4b. Fig. 4c shows the typical variation in the parison thickness, corresponding to the DSM action in Fig. 4b.

Modeling of Parison Formation

Due to the complex microstructure of molten polymers, modeling of annular flow in blow molding operations is governed neither by the current state of deformation nor by the current state of motion; instead, the overall stress field depends on the whole history of the deformation (19). Many existing models today are based either on molecular considerations or on modifications of established theories such as linear or non-linear viscoelasticity (20-22). In an extensive review, Crochet and Walters (23) presented the numerical simulation of the flow of highly elastic liquids in complex geometries. Brasseur et al. (24) solved the time-dependent compressible Newtonian extrudate-swell problem with slip at the wall, in an attempt to simulate the stick-slip extrusion instability. Tanoue and Iemoto (25) calculated the steady-state annular extrudate swell of polymer melts with die gap programming (VWDS) using the Giesekus constitutive model. The need for experimental trials to validate the simulations was emphasized. A neural network-based model approach was presented by Huang and Liao (26), in which the effects of the die temperature and flow rate on the diameter and thickness swell for HDPE were investigated. A good agreement was reported between experimentally determined parison swell and the predictions, at low flow rates, using the trained neural network model. In another work (27), they

presented a combination of finite element modeling using K-BKZ model (28-29) and artificial neural network (ANN) to predict the parison formation in extrusion blow molding. Their results showed that the die gap had a smaller effect on the diameter swell but a greater effect on the thickness swell. An increase in both diameter and thickness swell was reported by an increase in die angle. Huang et al. (30) used a hybrid method consisting of finite element method (FEM), artificial neural network (ANN), and genetic algorithm (GA) to find the optimal parison thickness distribution for a blow molded part with required thickness distribution. Recently, Mitsoulis (31) derived numerical solutions for the extrudate swell and exit correction in annular flow of pseudoplastic and viscoplastic fluids. Further studies based on the Herschel-Buckley model were proposed to improve the predictions for viscoelastic fluids (32). An extensive analysis of the existing approaches for the numerical simulation of non-Newtonian and viscoelastic fluids can be found elsewhere (33-34).

Governing Equations

To calculate the flow stresses in *BlowParison* software, the flow kinematics is derived using a generalized Newtonian model, and it is subsequently used as an input for the viscoelastic equation to calculate flow stresses (35). While the flow kinematics in the die was predicted based on the Hele-Shaw model, assuming Carreau viscosity model type behavior for the melt (37), the particle tracking as well as the deformation prediction was preformed using the K-BKZ viscoelastic model (27-29). Compared to the direct approach where the viscoelastic behavior of the material is taken into account from the beginning, this approach is more cost effective (36). That is, the calculation time is significantly reduced upon using the generalized Newtonian model as it does not require the calculation of the whole history of the deformation (19).

Flow in the Die: The viscosity takes the following form for a fluid obeying the Carreau model (37):

$$\eta = \eta_0 \cdot a_T \left[1 + \left(\lambda \cdot a_T \dot{\gamma} \right)^2 \right]^{\frac{n-1}{2}} \tag{10}$$

In this equation, η is the viscosity of the polymer melt at the processing temperature, η_0 is the zero-shear Newtonian viscosity at a reference temperature, $\dot{\gamma}$ is the shear rate, n is the power-law index for the shear-thinning zone, λ is a characteristic time representing the transition between the Newtonian and shear-thinning zones, and a_T is the temperature shift factor according to the WLF shift function (38-39).

Parison Formation after Exiting the Die: The K-BKZ model relates the stress to the strain history as follows (28-29):

$$\sigma(t) = -q\delta + \frac{1}{1-\theta} \int_{-\infty}^{t} \sum_{k=1}^{N} \left[m_k (t-\tau) \cdot h_k (I_1, I_2) \right] \left\{ c^{-1}(\tau, t) + \theta \cdot c(\tau, t) \right\} d\tau \tag{11}$$

where q is the hydrostatic pressure, δ is the identity tensor, t is the time, τ is the relaxation time, m is the memory function given by the Maxwell relaxation spectrum, k is the index of the linear-viscoelastic parameter sets for the memory function, N is the total number of the modes, c is the Cauchy deformation tensor, c^{-1} is the Finger deformation tensor, h is the damping function based on the invariants of the Finger tensor (I_1 and I_2), and θ is a parameter that refers to the second normal stress difference in the deformation (biaxial effect). The Papanastasiou damping function was used to represent the strain dependency under non-linear viscoelastic deformation (40-41):

$$h_k(I_1, I_2) = \frac{\alpha}{\alpha - 3 + \beta_k I_1(t,\tau) + \{1 - \beta_k\} I_2(t,\tau)} \tag{12}$$

In this equation, α and β are the damping coefficients. In this work, a total of 6 parameter sets were used for the constitutive model (N=6). The same value of α and β were used for all modes. The thermal dependence of the K-BKZ model was accounted for with the WLF temperature shift function.

The flow kinematics from the Carreau model was used as input to the K-BKZ model so as to calculate the flow stresses developed in the die. The overall stress components evaluated for each element were considered as the initial boundary conditions, knowing that these stresses were being removed at the moment the element emerged from the die. Therefore, the stress relaxation of the semi-solid extrudate was predicted based on the solid-mechanics principles. The distance in the die over which the particle tracking was performed had a pronounced effect on the swell prediction. Upon a wide range of experimental trials, this length was defined in a dimensionless form by the following expression:

$$L_{pt} = \left(\frac{D_{die}}{L_{die}}\right)^{a_1} \cdot \left[D_f \cdot S_1 + a_2 . \ln\left(DE^*\right)\right] \quad ; \quad 0 \le L_{pt} \le 1 \tag{13}$$

in this equation, a_1 and a_2 are constants, L_{die} is the die length, S_1 is a resin-dependent swell model parameter, DE^* is a modified Deborah number related to the flow time in the die (t_f) and terminal relaxation time of the resin (τ_t) as follows:

$$DE^* = \frac{\left(a_T \cdot \tau_t \cdot a_3\right)}{t_f} \tag{14}$$

where (3):

$$\tau_t = \eta_0 \cdot J_s^0 = \eta_0 \frac{\sum_{k=1}^{N} G_k \tau_k^2}{\left(\sum_{k=1}^{N} G_k \tau_k\right)^2} \tag{15}$$

and D_f is a parameter related to the die-head size, approaching unity for small die heads, according to the following correlation:

$$D_f = 1 - \left(\frac{a_4}{WE^*}\right) \quad ; \quad 0.1 \le D_f \le 1 \tag{16}$$

In the same manner as DE^*, the modified WE^* in Eq. 16 is defined as:

$$WE^* = \frac{\dot{Q} \cdot (a_T \cdot \tau_t \cdot a_3)}{A_{die} h_{die}} \tag{17}$$

where $\dot{Q}$ is the volumetric flow rate and A_{die} is the flow channel area at the die exit. In these equations, a_3 and a_4 are constants, a_T is the temperature shift factor, J_s^0 is the steady state compliance, and G_k and τ_k are the linear viscoelastic parameter sets for the memory function (relaxation moduli and relaxation times, respectively) given by the generalized Maxwell relaxation spectrum (N=6).

It is reported that the steady state compliance in Eq. 15 is independent of the average molecular weight, while it is strongly affected by the molecular weight distribution (3), and could be potentially related to various moments of the molecular weight distribution (3,42). Thus, in the absence of long-chain branching, it is hypothesized that by incorporating the terminal relaxation time as a parameter in the Hybrid approach, the polydispersity of HDPE grades could be accounted for in the swell prediction.

Mathematical Swell Model. The presented numerical formulation does not account for the elongational

forces developed at the entrance to the die and in the die land area. Moreover, the Hybrid fluid mechanics-solid mechanics approach presented in this work is based on the membrane elements for both the flow in the die and parison formation phase, which disregards the 3-dimentional nature of the shear flow in the die, particularly at high shear rates. These simplifications may not significantly affect the prediction of shear-dominated thickness swell at low flow rates (7,16), typical in fuel tank manufacturing operations. However, this could have a negative impact on the predicted diameter swell. To compensate for these shortcomings, the Hybrid approach is coupled with a mathematical swell model. This model makes use of dimensionless quantities (D_{die}/L_{die} aspect ratio and DE^* number) to compensate for the elongational forces ignored by the Hybrid approach. The swell model is developed based on a wide range of experimental trials conducted using different die geometries and operating conditions. This model identifies a hoop factor (HF) for each parison programming point, so as to compensate for the underestimated diameter swell. Therefore, the overall parison swell predicted for each element at each time-step is a combination of the numerically-predicted swell and the model-based hoop factor, defined as follows:

$$HF = C_H + C_R \cdot \frac{D_{die}}{L_{die}} \cdot \left(1 + DE^*\right) \tag{18}$$

In this equation, C_R and C_H are dimensionless die-geometry dependent and resin-dependent parameters, respectively, taking the following forms:

$$C_R = a_5 + \left(1 - a_5\right) \cdot \left(\frac{\phi_m - \phi_b}{45}\right) \tag{19}$$

$$C_H = \ln\left(\frac{\tau}{\tau_{ref}}\right) \tag{20}$$

where a_5 and τ_{ref} are constants, ϕ_m and ϕ_b are mandrel and bushing angles, respectively, and τ is the Maxwell relaxation time at the processing temperature. It should be mentioned that the mathematical swell model in *BlowParison* software has additional features to accommodate high flow rates, which could lead to pronounced thickness swell for the extruded parison. This software has been validated at high Weissenberg numbers (7), and is capable of predicting parison formation at high production rates (flow rates > 2000 g/s). The details of the Hybrid approach dealing with high Weissenberg numbers can be found elsewhere (7,16).

Modeling of Heat Transfer. Since a temperature gradient exists within a parison due to exposure to ambient air temperature, the heat is transported from the zones of higher temperature to that of lower temperature. If an energy balance is set up for a parison element, as the thickness is much lower than the other two dimensions, one obtains the differential equation for the temperature field as follows (43,44):

$$\rho \cdot C_p \frac{\partial T}{\partial t} = k \frac{\partial^2 T}{\partial x^2} \tag{21}$$

$$-k \frac{\partial T}{\partial x}\bigg|_{\Gamma} = h(T - T_\infty) \tag{22}$$

where ρ, C_p, and k are the density, specific heat and thermal conductivity of the resin, respectively, T is the parison temperature, x is the coordinate of the parison in the thickness direction, t is the elapsed time, h is the heat transfer coefficient at the boundary Γ, and T_∞ is the ambient air temperature.

EXPERIMENTAL

Material

A commercial linear HDPE blow molding resin, Basell Lupolen 4261A, was employed in this study. The resin was rheologically characterized to obtain the material parameters for the Carreau model and K-BKZ constitutive equation, and for the mathematical swell model.

Rheological Characterizations

Dynamic frequency sweep measurements were conducted on the molten resins on a Rheometrics ARES rheometer with a parallel plate setup. The measurements were conducted at three different melt temperatures on 25-mm diameter compression-molded disks. For each sample, frequency sweeps were made from 10^{-1} to 10^{2} rad/s at a strain of 10% (linear regime). The storage and loss moduli (G' and G'') and complex viscosity (η^*) curves were obtained as function of frequency (Fig. 5a). The relaxation times and moduli for the Maxwell relaxation spectrum (N=6) were estimated using the *UMat* software developed at IMI. The normalized damping curves were also constructed by dividing the G''/G' values at each frequency to the respective value at the highest frequency (10^2 rad/s). Figure 5b gives the normalized damping curve for the resin. The zero-shear Newtonian viscosity (η_0), Maxwell relaxation time (τ), and terminal relaxation time at the processing temperature ($a_T \cdot \tau_t$) are listed in Table 1.

To determine the strain-dependent part of the K-BKZ model in shear, stress relaxation experiments after a step strain were performed on a true-shear sliding-plate rheometer (Interlaken). The resin was characterized using this technique at 190 $^{\circ}C$ by imposing shear strains ranging from 0.05 to 10. The Papanastasiou damping coefficient α was calculated using the following equation (41):

$$h(I_1, I_2) = \left(\frac{\alpha}{\alpha + \gamma^2} \right) \tag{23}$$

where γ is the imposed shear strain. As the elongational forces in the Hybrid approach is accounted for by the swell model, the effect of the damping coefficient β was found to be negligible through a sensitivity analysis (results not shown). Hence, a default value of $\beta = 0.1$ was used in this study.

The swell parameter S_1 (Eq. 13) was estimated based on a correlation developed at IMI (16). Knowing that a significant decay of the normalized damping curve as a function of frequency represents a more dominant loss modulus at high temperatures, this correlation relates the swell parameter S_1 to the slope of its normalized damping curve (Fig. 5b) as follows:

$$S_1 = p_1 \cdot \ln(n_d) + p_2 \tag{24}$$

where p_1 and p_2 are the correlation parameters, and n_d is the absolute value of the slope calculated for the normalized damping curve (Fig. 5b). The higher the slope is, a more pronounced sagging and a less significant swelling is expected for the resin, leading to a reduced value for the swell parameter S_1 . All the estimated material parameters are listed in Table 1.

Parison Formation Trials

The resin was extruded on a continuous industrial-scale extruder at Kautex Inc. using four diverging die geometries and different sets of operating conditions. Figure 6 gives the die geometries considered in these studies, denoted as I to IV. The die length and bushing diameter, as well as the minimum die gap, are displayed in this Figure. All die heads had a bushing angle of 10° and a mandrel angle of 30°, featuring the same die land length (35 mm). The target parison length was achieved by adjusting the extrusion time for the given number of VWDS and PWDS programming points (*NPPt*=64). Table 2 gives the operating conditions for these trials, denoted as (a) to (d).

For comparing the experimental and predicted weight swell profiles, the definition of parison weight without swell (w_0) in Eq. 4 was identified to be too simplistic, due to the complex shape of the extruded parisons created by VWDS/PWDS die gap manipulations. Therefore, the following equation was used to estimate the overall weight without swell for the extruded parison:

$$w_0 = \sum_{ippt=1}^{NPPt} \left[\left(\frac{A_{ippt} + A_{ippt-1}}{2} \right) \cdot L_{ippt} \cdot \left(\frac{L_{parison}}{L_0} \right) \cdot \rho \right] \tag{25}$$

and the overall weight with swell and sag for a continuous extrusion was defined as:

$$w = \sum_{ippt=1}^{NPPt} \dot{w} \cdot \left(t_{ippt} - t_{ippt-1} \right) = \dot{w} \cdot t_{ext} \tag{26}$$

In these equations, $\dot{w}$ is the experimental mass flow rate, t_{ext} is the total extrusion time, t_{ippt-1} and t_{ippt} are the extrusion times at two consecutive VWDS/PWDS programming points, ρ is the melt density, and $L_{parison}$ is the final parison length with swell and sag. In Eq. 25, A_{ippt-1} and A_{ippt} are the flow channel areas at two consecutive programming points after VWDS/PWDS actions, without swell and sag, and L_{ippt} is the extruded parison segment length between t_{ippt-1} and t_{ippt}, without swell and sag, calculated by IMI's parison mesh generation software (*ParMesh*: See **Numerical Simulations**). It should be mentioned that the term ($L_{parison}/L_0$) in Eq. 25 is introduced in an effort to compare the weight for the same parison length before and after swell (see Eq. 4), where L_0 is the total parison length without swell and sag calculated by *ParMesh* software. Due to the mass balance conservation, it can be seen that by incorporating the Eqs. 25 and 26 in Eq. 4, the weight swell can be simply reduced to:

$$B_w = \frac{L_0}{L_{parison}} \tag{27}$$

For the trial (c), the final blown part was also axially dissected into 10 sections with equal lengths. The sections were weighed and the values were compared to the predicted section weights coming from the simulations.

NUMERICAL SIMULATIONS

IMI's *ParMesh* software was used to create the finite element mesh of the die and the initial parison mesh, without swell and sag, for given sets of VWDS/PWDS profiles and input die geometry information (Eqs. 5-9). The die mesh contained 9600 "3-node" membrane elements in all cases (Fig. 6). Depending on the parison length, 18000 to 25000 membrane elements were used to create the finite element mesh of the parison. The parison formation, accounting for swell and sag as well as the non-isothermal effects, was subsequently predicted using *BlowParison* software.

RESULTS AND DISCISSION

Initial Parison without Swell and Sag

Figure 7a shows the initial parison mesh generated using *ParMesh* software for the four trials (both front and back views). While the axial variation in the thickness profile is created by VWDS programming, the circumferential thickness variation is produced by PWDS manipulations. The front and back views of the final blown parts are shown in Fig. 7b. The irregular shape of the fuel tanks in these pictures clearly explains the need for the combined VWDS/PWDS actions. For the four trials, the flow channel area as a function of VWDS/PWDS programming points, calculated by *ParMesh* software, is given in Fig. 8a. In this figure, *ippt*=1 corresponds to the parison bottom section while *ippt*=64 represents the

uppermost section at the die exit. The increase in the flow channel area for the particular sections of the fuel tanks is meant to compensate for the higher blow-up ratio in these zones. The corresponding parison length evolution, without swell and sag (L_0), as a function of extrusion time is presented in Fig. 8b. Despite much shorter extrusion time in the trial (a), the initial parison is much longer compared to the other cases because of the lower VWDS/PWDS actions used for this small die, and also due to its lower minimum gap (h_{min} in Fig. 6). To compare the circumferential thickness distribution of the initial parisons, the highest PWDS pull and/or push actions used for the four trials as function of circumferential die angle are presented in Figs. 8c and 8d. These ultimate values correspond to the middle axial zone of the parts. It can be seen that up to 3.5 mm of PWDS pulling action, leading to the same amount of circumferential increase in the die gap, is required so as to compensate for the irregular part shape in the trial (d).

Mathematical Swell Model

For the four trials, Figs. 9a and 9b give the swell model variables L_{pt} and HF, respectively, as function of DE^* number. With the exception of the die I, the dimensionless distance used in the particle tracking (L_{pt}) increases with decreasing die head size, primarily because the flow time in the die reduces for smaller die heads (see Eqs. 13-14 and Fig. 6). The reduced L_{pt} value for the die I is mainly attributed to its lower D_{die}/L_{die} aspect ratio, according to Eq. 13. In Fig. 9b, the hoop factor (HF) increases monotonically with decreasing die head size. Given the lower minimum gap for the smaller die heads (Fig. 6), the flow time in the die reduces while the elongational forces in the die land area tend to increase as a result of a higher contraction in the die land zone. This leads to a more pronounced diameter swell for the dies I and II. The increased diameter swell for the die I is also attributed to the higher mass flow rate in the die. All these factors result in a higher HF, via enhancing DE^* in Eq. 18.

Comparison between Experimental Results and Numerical Predictions

Fig. 10 shows the simulated parisons using *BlowParison* software for the four trials. It can be seen that the final parison lengths in all cases are very similar regardless of the pronounced differences in their respective initial parison lengths, without swell and sag (see Figs. 7a and 8b). This implies a more significant swelling in trials (a) and (b). As mentioned before, this is primarily attributed to the higher contraction in the die land zone for the dies I and II, and to some extent, to the more drastic changes in the die diameter along the flow channel. Hence, because of the resin memory, the parison tends to regain the diameter it originally had at the die entrance, leading to a pronounced sudden diameter swelling in both cases (hoop stresses). Moreover, the smaller h_{min} also leads to more pronounced shear stresses in the die land zone for these dies. It has been shown that this kind of contracting configuration could cause a significant thickness swell for the extruded parison (7,16). Therefore, the resulting weight swell is higher for these dies, as brought in Table 2. A comparison between the predicted and experimental length and weight swell data in Table 2 shows less than 5% error in all cases, demonstrating that the Hybrid approach used here is capable of discriminating between the effect of die geometry and die gap profile on the final parison swell. Future work will focus on the potential of comparing the predicted parison dimension with the experimental data coming from a pinch off mold for these parts. This will also provide more insight into the validity of some assumptions taken here to relate the geometrical and processing parameters to the variables of the mathematical swell model.

Figure 11 compares the experimental and simulated weight profiles for the dissected final part (case c). A very good agreement can be seen between the two, showing the validity of the predictions for part design purposes. The current practice for designing new parts could be quite time consuming due to the complex nature of the swell and sag characteristics for the part produced by die gap manipulation techniques. A modeling tool that could predict the parison dimensions upon any variations in the die

geometry, die gap programming, resin characteristics, and operating conditions could significantly reduce the part design times and costs (16). More validation data on the successful use of the presented modeling tool for a multitude of complex industrial parts can be found elsewhere (14).

Figure 12 shows the predicted temperature distribution at the outer surface of the parison for the four trials (T_∞ = 20 °C & h = 5 W/m^2/°C). It can be seen that the temperature drop at the bottom is proportional to the extrusion time (t_{ext}: see Table 2). Since the memory function in the K-BKZ model is temperature dependent (Eq. 11), the higher the extrusion time, the higher the parison swelling at the bottom due to a more pronounced temperature drop. In light of this, a higher swelling at the bottom is quite expected because of both time-dependent swelling and non-isothermal effects, as it can be seen in Fig. 10.

CONCLUSION

This work presented the strong dependence of parison dimensions on die geometry and die gap manipulation (VWDS/PWDS). IMI's *ParMesh* software was used to create the finite element mesh of the initial parison, without swell and sag, for given sets of VWDS/PWDS profiles and input die geometry information. IMI's *BlowParison* software was subsequently used to predict the parison formation, taking into account the swell and sag, as well as the non-isothermal effects. The comparison between the predicted parison dimensions and experimental data demonstrated the capability of this modeling tool in predicting the parison length and weight profiles. In light of this, the parison dimensions from simulation could be readily used as the starting point for process design, reducing the part design times and costs and customer delivery time. This work also demonstrated that a modeling approach capable of creating the link between the die gap manipulation and parison swell and sag could be the key to a better control over the thickness distribution for the final part. Future work will focus on

the potential of comparing the predicted parison dimensions with the experimental data coming from a pinch-off mold. This will also provide more insight into the validity of some assumptions taken here to relate the geometrical and processing parameters to the variables of the mathematical swell model.

ACKNOWLEDGEMENT

The authors would like to thank Stephanie Chang and Marc-André Rainville for their technical contribution. Special thanks go to the members of the IMI's SigBlow consortium for their continuing support and Kautex Inc. for providing experimental data for validation of the IMI's modeling software.

REFERENCES

1. D.V. Rosato, D.V. Rosato, *Blow Molding Handbook*, Hanser Publishers, New York (1989).
2. H.X. Huang, Y.Z. Lia Y.H. Denga, *Polymer Testing*, **25**, 839 (2006).
3. J.M. Dealy, K.F. Wissbrun, *Melt Rheology and its Role in Plastics Processing*, Van Nostrand Reinhold (1990).
4. N. Orbey, J.M. Dealy, *Polym. Eng. Sci.*, **24**, 511 (1984).
5. V.I. Brizitsky, G.V. Vinogradov, A.I. Isayev, Y.Y. Podolsky, *J. Appl. Polym. Sci.*, **27**, 751 (1978).
6. N. Sheptak, C.E. Beyer, *SPE J.*, **21**, 190 (1965).
7. A.M. Yousefi, P. Collins, S. Chang, R.W. DiRaddo, *Polym. Eng. Sci.*, **47**, 1 (2007).
8. R.J. Koopmans, *Polym. Eng. Sci.*, **32**, 1741 (1992).
9. R.J. Koopmans, *Polym. Eng. Sci.*, **32**, 1750 (1992).
10. R.J. Koopmans, *Polym. Eng. Sci.*, **32**, 1755 (1992).
11. A.M. Yousefi, D. Laroche, P. Collins, R. DiRaddo, *SPE Blow Molding Division newsletter* (Spring 2003).
12. A.M. Yousefi, P. Collins, R. DiRaddo, *SPE ANTEC Tech. Papers*, Nashville (2003).
13. A.M. Yousefi, D. Laroche, P. Collins, R. DiRaddo, *6th EsaForm Conference*, Salerno, Italy (2003).
14. P. Debergue, D. Laroche, A.M. Yousefi, R. DiRaddo, H. Atsbha, *24th Annual Meeting of the Polymer Processing Society (PPS-24)*, Salerno, Italy, June 15-19 (2008).
15. F. Thibault, A.M. Yousefi, R.W. DiRaddo, H. Atsbha, *PPS-22 Conference*, Yamagata, Japan (2006).
16. A.M. Yousefi, J. den Doelder, M.A. Rainville, K.A. Koppi, submitted to *Polym. Eng. Sci.* (2008).

17. R.W. DiRaddo, A. Garcia-Rejon, L. Pecora, D.Poirier, *SPE ANTEC Tech. Papers*, 1026 (1994).

18. M. Thielen, *SPE-ANTEC Technical papers*, Orlando, 863 (2000).

19. M. Renardy, *J. Non-Newt. Fluid Mech.*, **90**, 243 (2000).

20. M. Renardy, *Ann. Rev. Fluid Mech.*, **21**, 21 (1989).

21. R.S. Graham, T.C.B. McLeish, *J. Rheol*, **45**, 275 (2001).

22. T.C.B. McLeish, R.G. Larson, *J. Rheol*, **42**, 81 (1998).

23. M.J. Crochet, K. Walters, *Ann. Rev. Fluid Mech.*, **15**, 241 (1983).

24. E. Brasseur, M.M. Fyrillas, G. Georgios, M.J. Crochet, *J. Rheol*, **42**, 549 (1998).

25. S. Tanoue, Y. Iemoto, *Polym. Eng. Sci.*, **39**, 2172 (1999).

26. H.X. Huang, C.M. Liao, *Polymer Testing*, **21**, 745 (2002).

27. H.X. Huang, Y.S. Miao, *Trans. ASME*, **129**, 218 (2007).

28. A. Kaye, *College of Aeronautics*, Cransfield, Note No.134 (1962).

29. B. Bernstein, E. Kearsley, L.J. Zapas, *Trans. Soc. Rheol.*, **7**, 391 (1963).

30. G.Q. Huang, H.X. Huang, *J. Mater. Proc. Tech.*, **182**, 512 (2007).

31. E. Mitsoulis, *J. Non-Newt. Fluid Mech.*, **141**, 138 (2007).

32. E. Mitsoulis, S.S. Abdali, N.C. Markatos, *Can. J. Chem. Eng.*, **71**, 147 (1993).

33. M.J. Crochet, A.R. Davies, K. Walters, *Numerical Simulation of Non-Newtonian Flow*, Elsevier, New York, (1984).

34. J.A. Brydson, *Flow Properties of Polymer Melts*, George Godwin Ltd., London (1981).

35. L. Douven, *PhD thesis*, Technische Universiteit Eindhoven, The Netherlands (1991).

36. F. P. T. Baaijens, *Rheol. Acta*, **30**, 284 (1991).

37. C.L. Tucker III, *Computer Modeling for Polymer Processing – Fundamentals*, Hanser Publishers (1989).

38. M.L. Williams, R.F. Landel, J.D. Ferry, *J. Am. Chem. Soc.*, **77**, 3701 (1955).

39. K.K. Kabanemi, J.F. Hetu, A. Garcia-Rejon, *Intern. Polym. Proc.*, **12**, 182 (1997).

40. X.L. Luo, R.I. Tanner, *Int. J. Num. Meth. Eng.*, **25**, 9 (1988).

41. A.C. Papanastasiou, L.E. Scriven, C.W. Macosko, *J. Rheol.*, **27**, 387 (1983).

42. M. Kurata, *Macromolecules*, **17**, 895 (1984).

43. F.P. Incropera, D.P. De Witt, *Introduction to Heat Transfer*, John Wiley & Sons, New York (1985)

44. A. Yousefi, A. Bendada, R. Diraddo, *Polym. Eng. Sci.*, 42, 1115 (2002).

FIGURE LEGENDS

FIG. 1. (a) Schematic representation of the VWDS technique at different mandrel positioning; (b) VWDS stroke parameters used in the industry to control the die gap opening; (c & d) mandrel positioning at 0% and 100% VWDS programming, respectively.

FIG. 2. Schematic representation of the SFDR technique; (a) original die gap with no SFDR action (b) original die gap between 90° and 270° with SFDR action outside this range; (c) original die gap between 180° with SFDR action everywhere else. The activated SFDR components are in a dark color.

FIG. 3. Schematic representation of the PWDS technique; (a) original die gap with no PWDS action (b) original die gap at 180° with PWDS pushing action at 0°; (c) original die gap at 180° with PWDS puling action at 0°; (d) variation in the die gap caused by PWDS pulling action at 0° at as a function of circumferential die angles (case c). The activated PWDS components are in a dark color (b & c).

FIG. 4. Schematic representation of the DSM technique; (a) original die gap with no DSM action (b) DMS pulling action between 0° – 30° and 220° – 250°. The activated DSM components are in a dark color. (c) Typical variation in the parison thickness corresponding to the DSM pulling action in case b.

FIG. 5. (a) Elastic and loss modulus (G' & G'') and complex viscosity (η^*) curves; (b) normalized damping curve as function of frequency obtained using a parallel-plate rheometer.

FIG. 6. Die geometries examined in this work. The scale bar shows the flow time in the die (in seconds) calculated by the fluid-mechanics component of the Hybrid approach. The bushing diameter, die length, and minimum gap (h_{min}) are identified for each die. $\phi_b = 10°$, $\phi_m = 30°$, $L_{dl} = 35$ mm.

FIG. 7. (a) Front and back views of the initial parison mesh, without swell and sag, created by *ParMesh* software for the four trials. The scale bar shows the parison thickness distribution created by

VWDS/PWDS techniques. The parison lengths without swell and sag (L_0) and the total parison weights (w) are displayed. (b) Corresponding front and back views of the final part geometries for these trials.

FIG. 8. (a & b) Flow channel area and parison length evolution, respectively, without swell and sag, as a function of VWDS programming points calculated by *ParMesh* software. (c & d) Highest PWDS pull or push actions used for the four trials as function of circumferential die angle. These ultimate values correspond to the middle axial zone of the parts (see Fig. 6b).

FIG. 9. Swell model variables estimated for the 4 trials; (a) dimensionless distance used in the particle tracking as a function of DE^* number; (b) Swell factor HF as a function of DE^* number. The values are calculated at the respective flow rates for these trials and at the minimum die gap for the 4 dies.

FIG. 10. Front and back views of the simulated parison formation, with swell and sag, using *BlowParison* software for the four trials, respectively. The scale bar shows the final parison thickness distribution.

FIG. 11. Comparison between the experimental and predicted weight profile for the dissected final part with flash (trial c).

FIG. 12. Predicted temperature distribution at the outer surface of the parison for the four trials (T_∞ = 20 °C & h = 5 W/m^2/°C). The temperature at the bottom drops proportional to the extrusion time (t_{ext}: see Table 2);

Table 1. Zero-shear Newtonian viscosity (η_0), damping coefficients (α & β), Maxwell and terminal relaxation times at the processing temperature (τ & $a_T.\tau_t$), swell model parameter (S_1), thermal properties (C_p & k), melt density (ρ), and K-BKZ fits for Basell HDPE Lupolen-4261 resin.

Material Properties		**K-BKZ model fits**	
η_0 (MPa.s)	0.21	G_k (MPa) & τ_k (s)	
α	16.0		
β	0.1		
τ (s)	1.0	0.300	0.006
$a_T \cdot \tau_t$ (s)	32.0	0.122	0.035
S_1	0.46	0.065	0.207
C_p (J/kg/ °C)	2700	0.027	1.220
k (W/m/°C)	0.23	0.009	7.170
ρ (g/cm^3)	0.746	0.005	42.15

Table 2. Operating conditions used for the parison formation trials. The experimental and predicted parison length and weight swell results are also compared.

Trial	Die	T_{melt} ($^{\circ}C$)	$^{*}T_{\infty}$ ($^{\circ}C$)	$\dot{w}$ (g/s)	t_{ext} (s)	Die Gap Manipulation	Parison Length (mm)		Weight Swell (B_w)	
							Exp.	Sim.	Exp.	Sim.
(a)	I	205	20	268	51	VWDS - PWDS	1440	1508	2.03	1.94
(b)	II	205	20	173	100	VWDS - PWDS	1670	1664	1.80	1.80
(c)	III	205	20	158	95	VWDS - PWDS	1570	1507	1.08	1.13
(d)	IV	205	20	166	120	VWDS - PWDS	1530	1602	1.01	0.96

* $h = 5$ W/m^2/°C

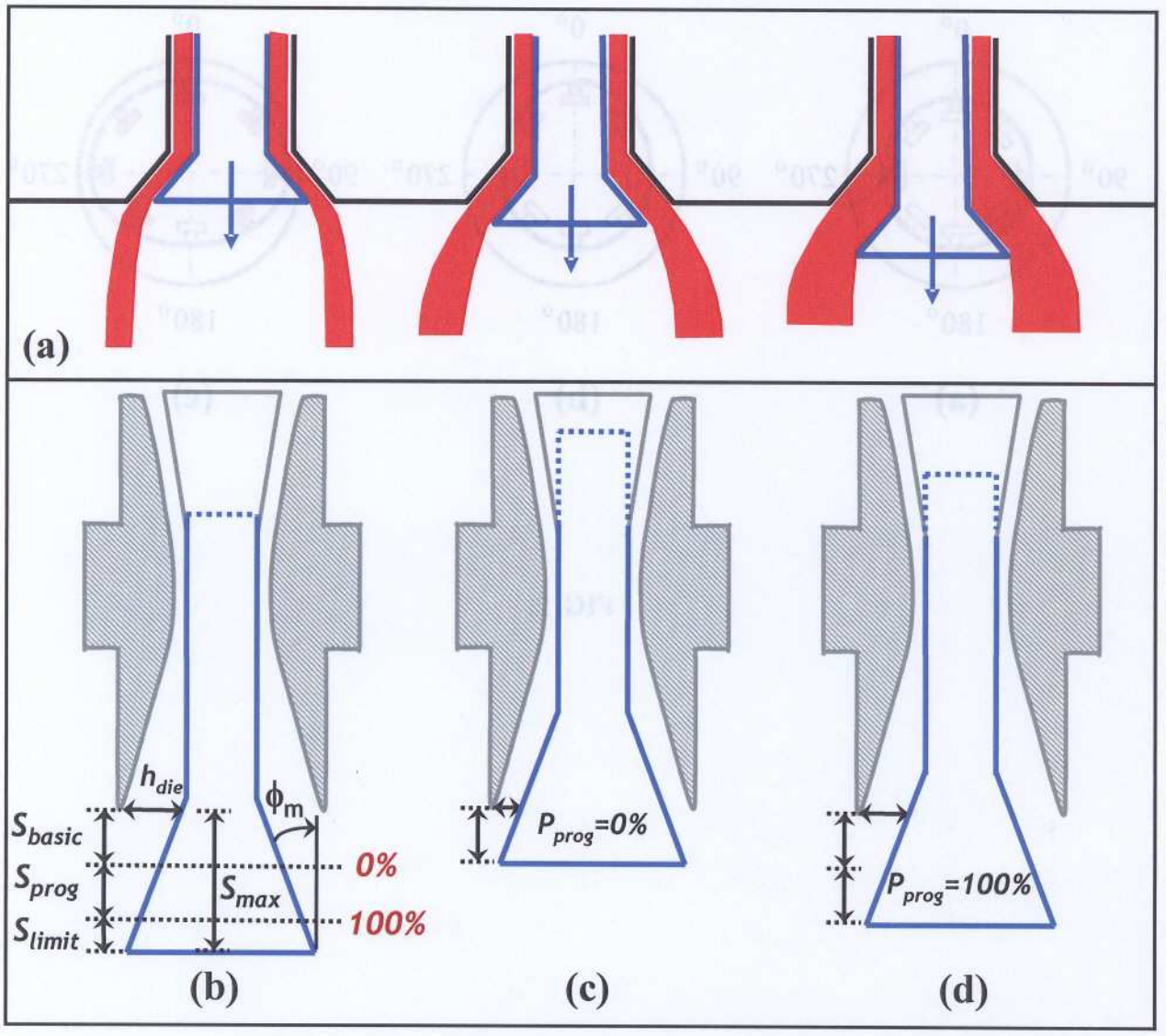
(a)
h_{die}
ϕ_m
S_{basic}
S_{prog}
S_{limit}
S_{max}
0%
100%
P_{prog}=0%
P_{prog}=100%
(b)
(c)
(d)

FIG. 1.

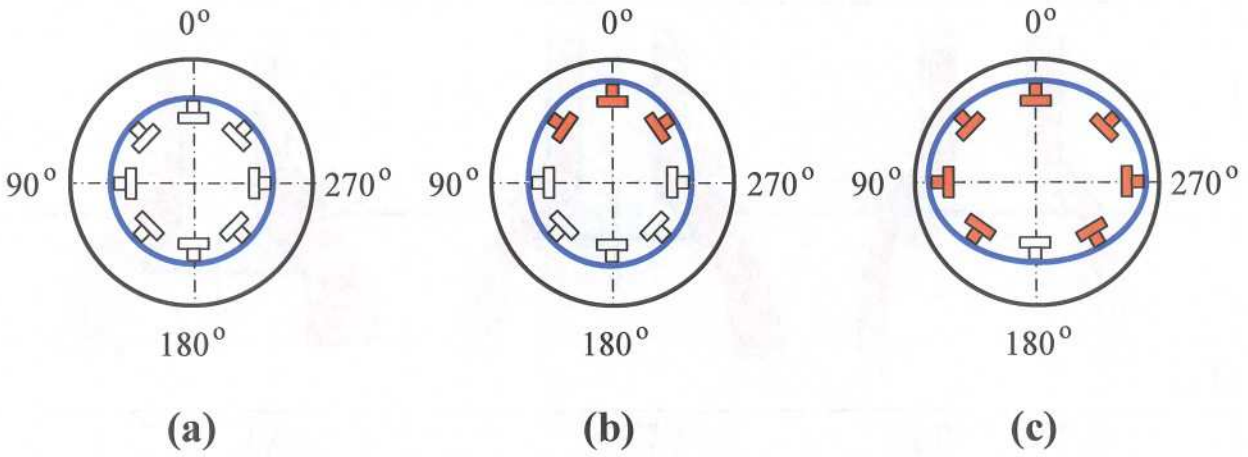

FIG. 2.

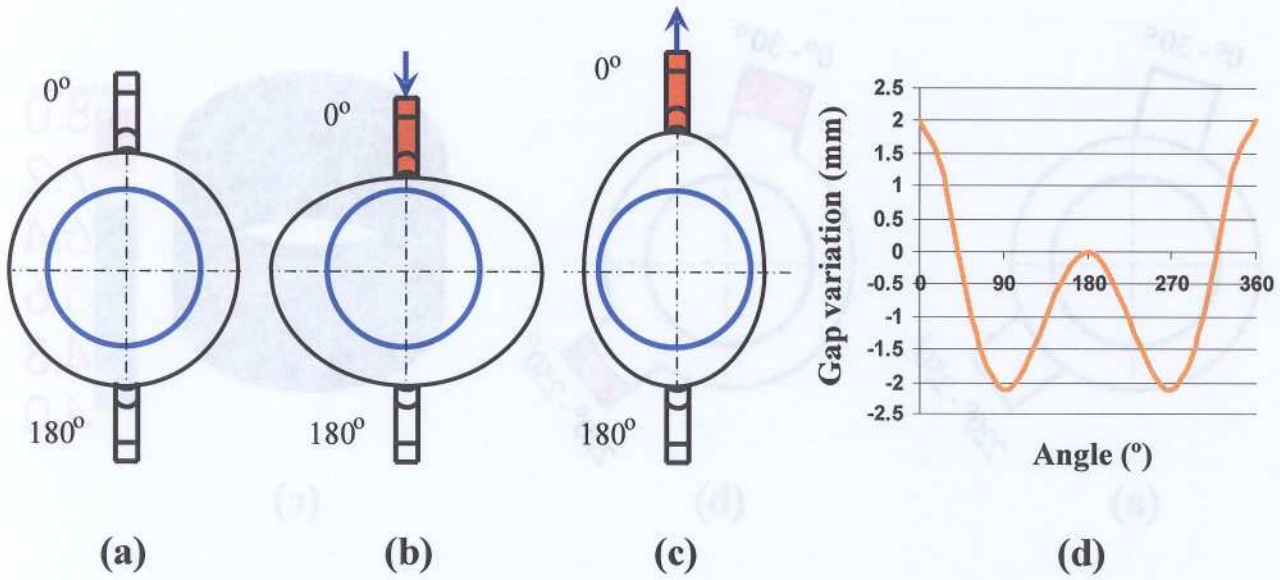
0°
180°
0°
180°
0°
180°
Gap variation (mm)
2.5
2
1.5
1
0.5
0
-0.5
-1
-1.5
-2
-2.5
0
90
180
270
360
Angle (°)
(a)
(b)
(c)
(d)

FIG. 3.

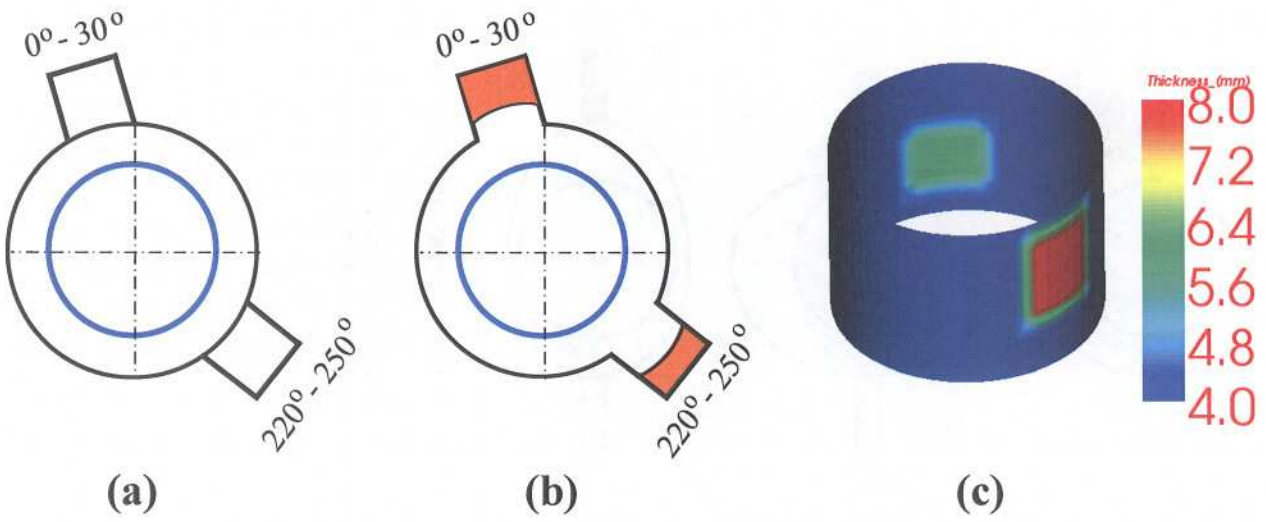

FIG. 4

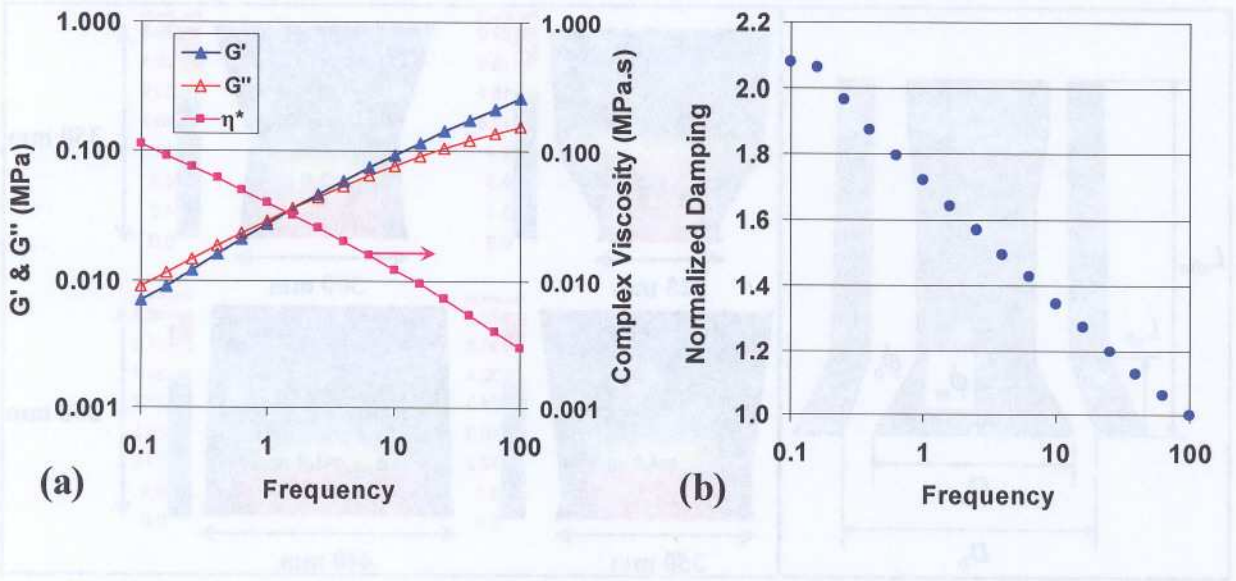
1.000
0.100
0.010
0.001
G' & G'' (MPa)
G'
G''
η*
Complex Viscosity (MPa.s)
0.1
1
10
100
Frequency
(a)
2.2
2.0
1.8
1.6
1.4
1.2
1.0
Normalized Damping
(b)

FIG. 5.

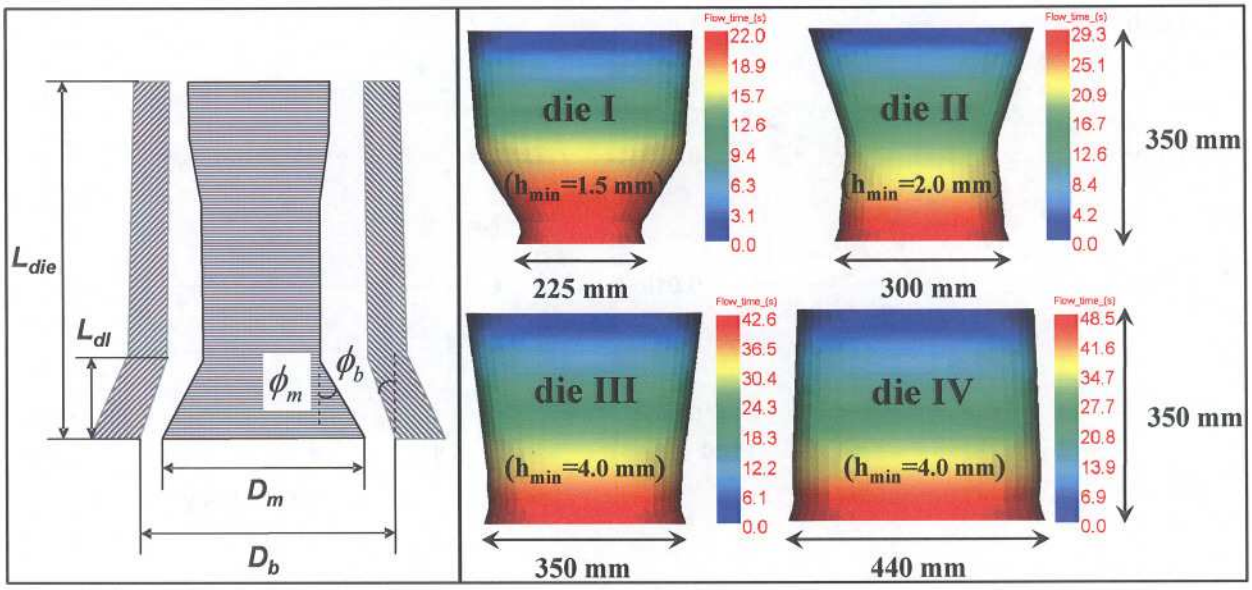
L_{die}
L_{dl}
ϕ_m
ϕ_b
D_m
D_b
die I
(h_{min}=1.5 mm)
225 mm
Flow_time_(s)
22.0
18.9
15.7
12.6
9.4
6.3
3.1
0.0
die II
(h_{min}=2.0 mm)
300 mm
Flow_time_(s)
29.3
25.1
20.9
16.7
12.6
8.4
4.2
0.0
350 mm
die III
(h_{min}=4.0 mm)
350 mm
Flow_time_(s)
42.6
36.5
30.4
24.3
18.3
12.2
6.1
0.0
die IV
(h_{min}=4.0 mm)
440 mm
Flow_time_(s)
48.5
41.6
34.7
27.7
20.8
13.9
6.9
0.0
350 mm

FIG. 6.

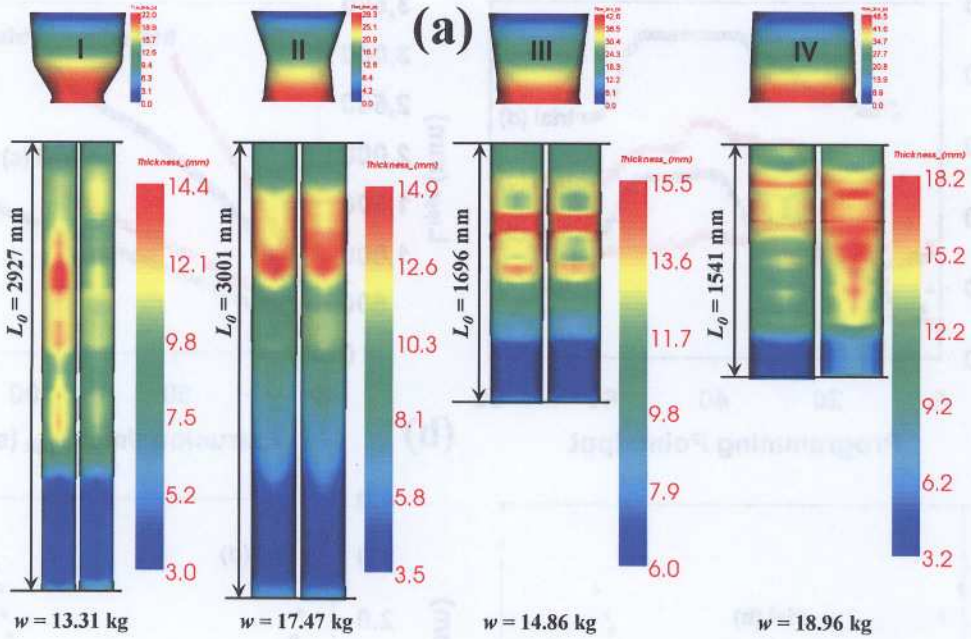
(a)
I
II
III
IV
L_0 = 2927 mm
L_0 = 3001 mm
L_0 = 1696 mm
L_0 = 1541 mm
14.4
12.1
9.8
7.5
5.2
3.0
14.9
12.6
10.3
8.1
5.8
3.5
15.5
13.6
11.7
9.8
7.9
6.0
18.2
15.2
12.2
9.2
6.2
3.2
w = 13.31 kg
w = 17.47 kg
w = 14.86 kg
w = 18.96 kg

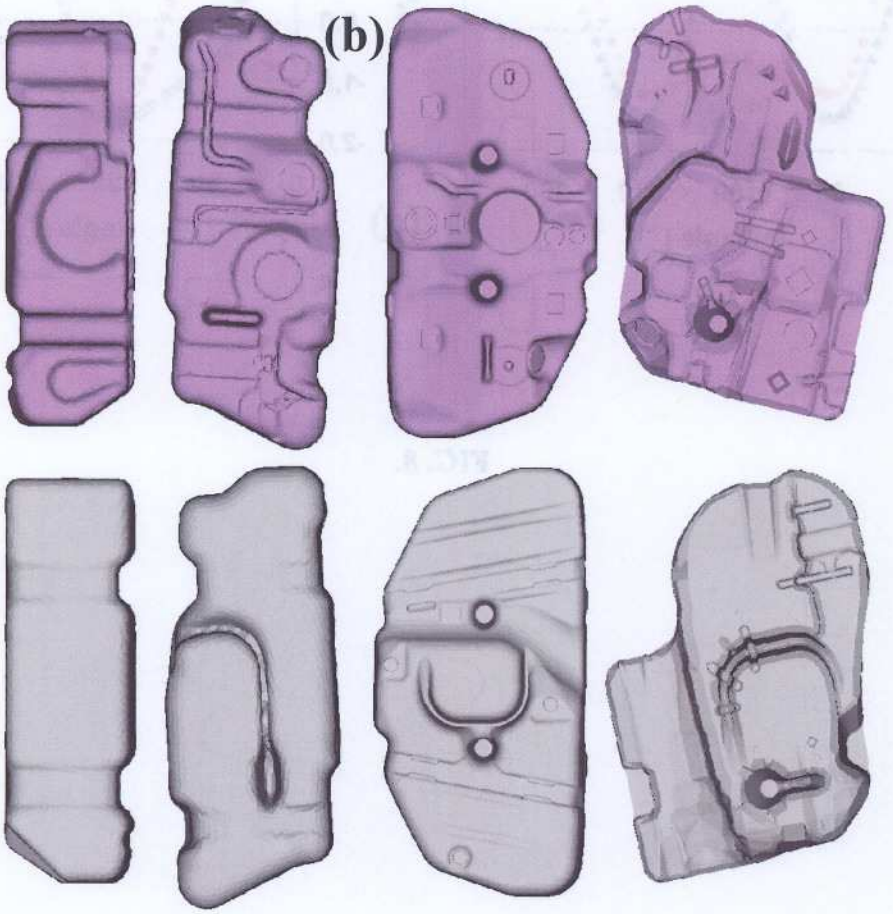
(b)

FIG. 7.

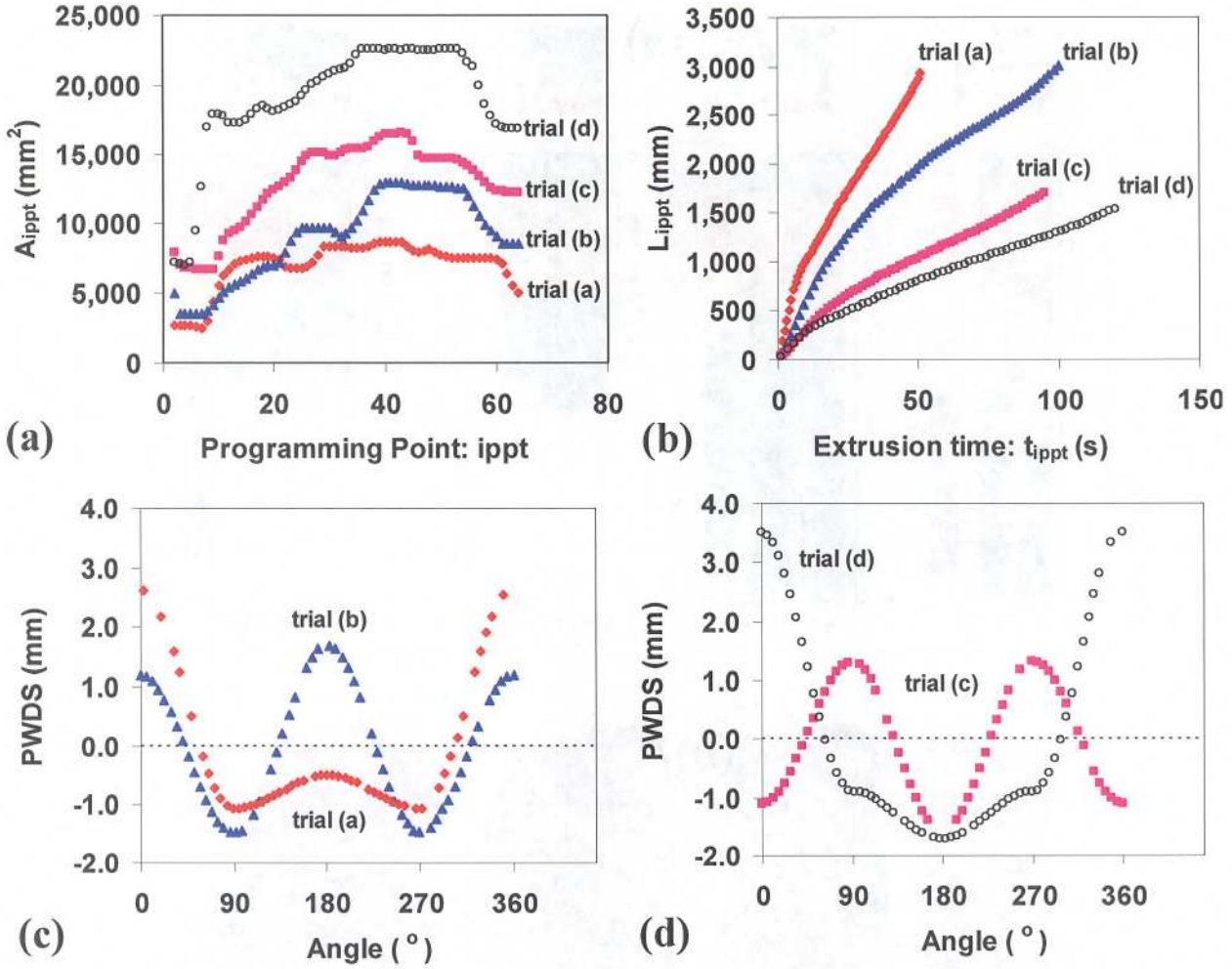
25,000
20,000
15,000
10,000
5,000
0
A_{ippt} (mm^2)
trial (d)
trial (c)
trial (b)
trial (a)
0
20
40
60
80
Programming Point: ippt
(a)
3,500
3,000
2,500
2,000
1,500
1,000
500
0
L_{ippt} (mm)
trial (a)
trial (b)
trial (c)
trial (d)
0
50
100
150
Extrusion time: t_{ippt} (s)
(b)
4.0
3.0
2.0
1.0
0.0
-1.0
-2.0
PWDS (mm)
trial (b)
trial (a)
0
90
180
270
360
Angle (°)
(c)
4.0
3.0
2.0
1.0
0.0
-1.0
-2.0
PWDS (mm)
trial (d)
trial (c)
0
90
180
270
360
Angle (°)
(d)

FIG. 8.

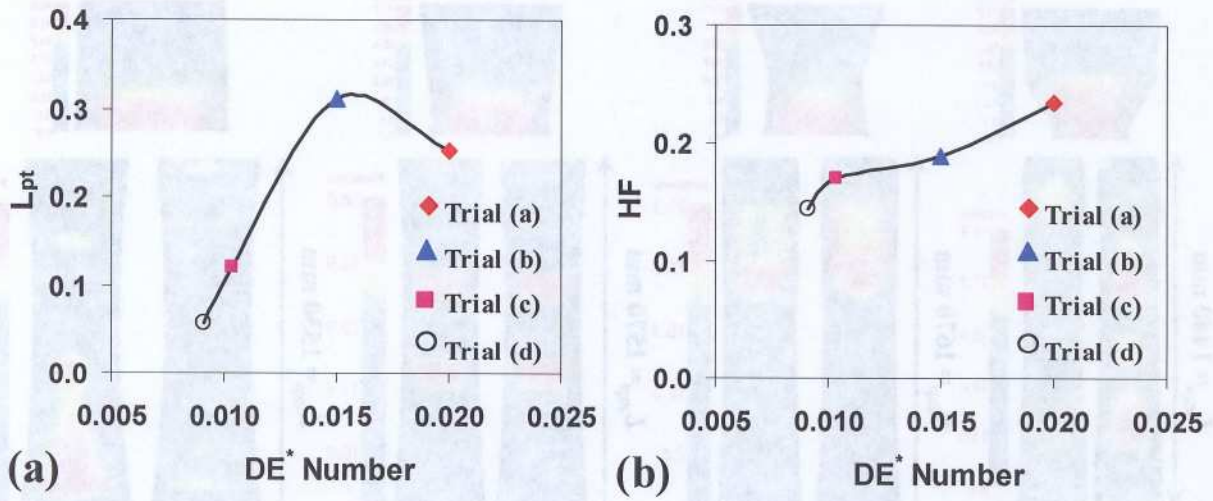
0.4
0.3
0.2
0.1
0.0
L_{pt}
0.005
0.010
0.015
0.020
0.025
DE* Number
Trial (a)
Trial (b)
Trial (c)
Trial (d)
(a)
0.3
0.2
0.1
0.0
HF
0.005
0.010
0.015
0.020
0.025
DE* Number
Trial (a)
Trial (b)
Trial (c)
Trial (d)
(b)

FIG. 9.

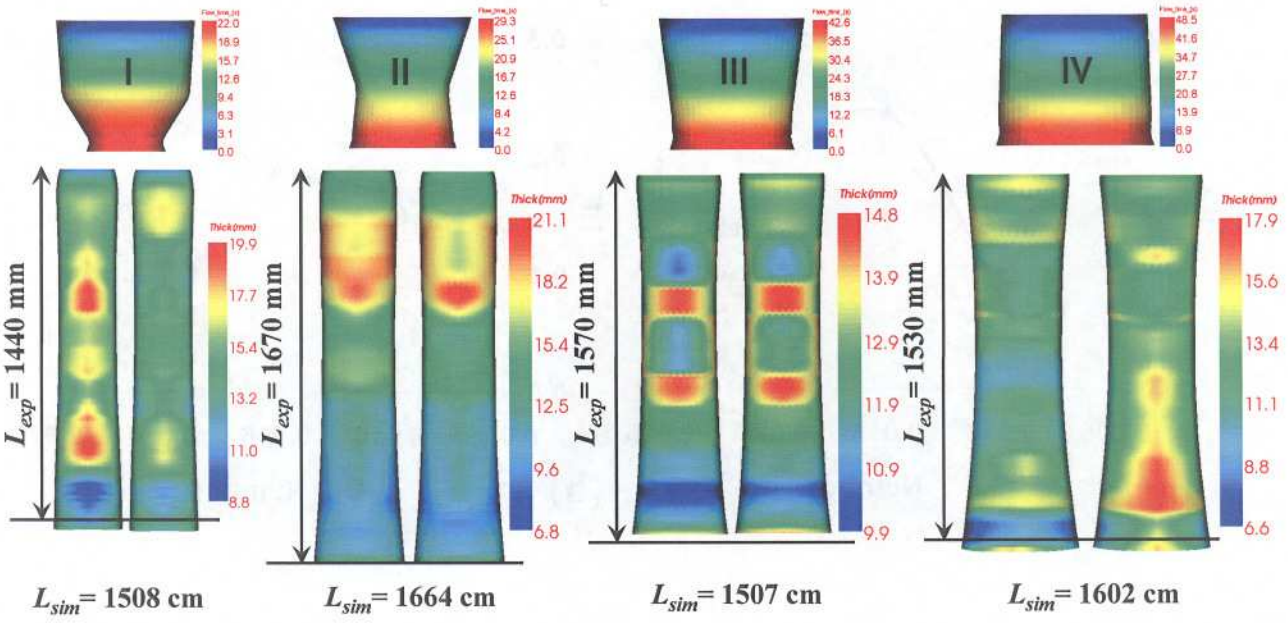
I
II
III
IV
L_{exp} = 1440 mm
L_{exp} = 1670 mm
L_{exp} = 1570 mm
L_{exp} = 1530 mm
Thick(mm)
L_{sim} = 1508 cm
L_{sim} = 1664 cm
L_{sim} = 1507 cm
L_{sim} = 1602 cm

FIG. 10.

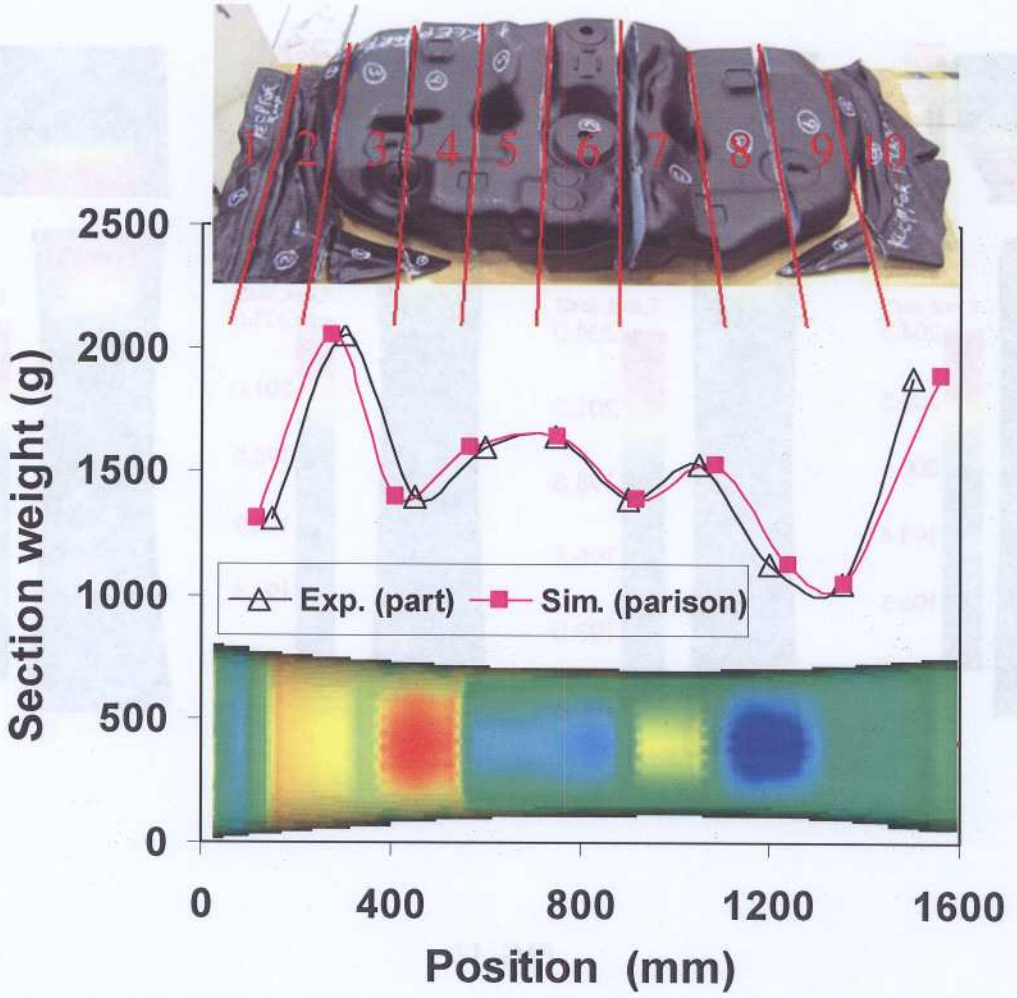
1
2
3
4
5
6
7
8
9
10
2500
2000
1500
1000
500
0
Section weight (g)
Exp. (part)
Sim. (parison)
0
400
800
1200
1600
Position (mm)

FIG. 11.

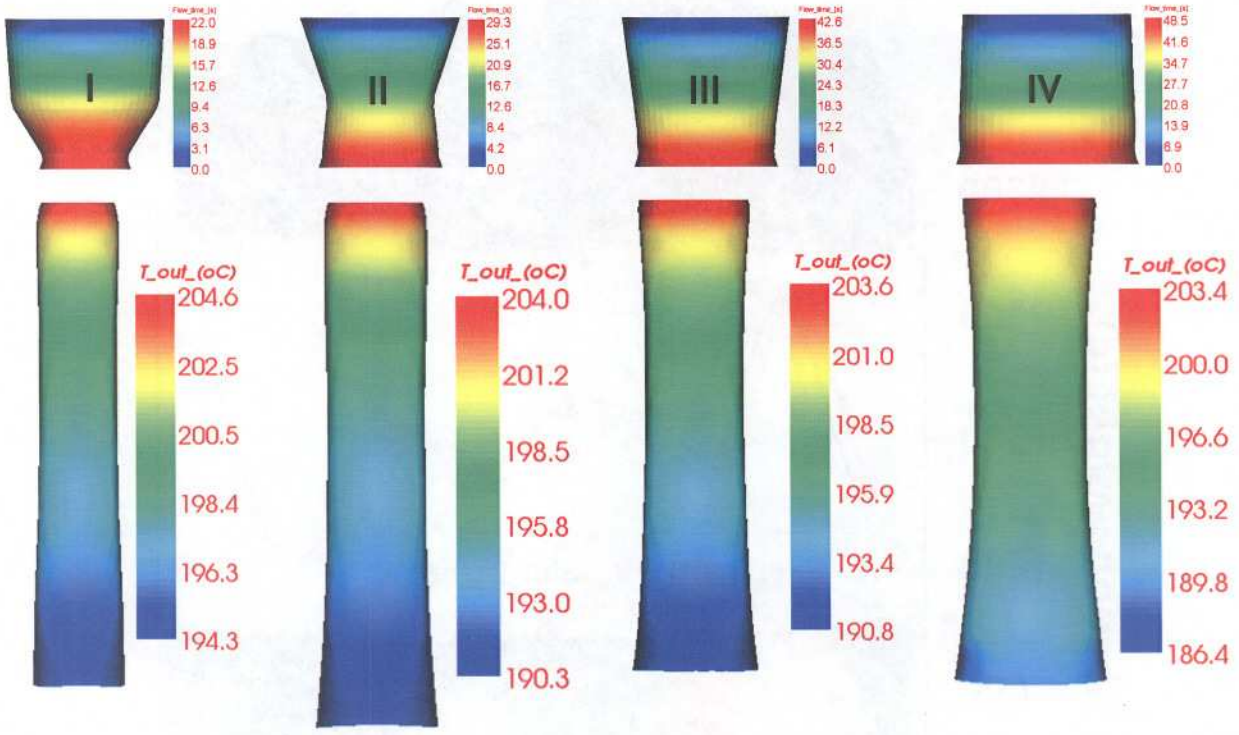
I
22.0
18.9
15.7
12.6
9.4
6.3
3.1
0.0
T_out_(oC)
204.6
202.5
200.5
198.4
196.3
194.3
II
29.3
25.1
20.9
16.7
12.6
8.4
4.2
0.0
T_out_(oC)
204.0
201.2
198.5
195.8
193.0
190.3
III
42.6
36.5
30.4
24.3
18.3
12.2
6.1
0.0
T_out_(oC)
203.6
201.0
198.5
195.9
193.4
190.8
IV
48.5
41.6
34.7
27.7
20.8
13.9
6.9
0.0
T_out_(oC)
203.4
200.0
196.6
193.2
189.8
186.4

FIG. 12.